Optical nanotopography of fluorescent surfaces by axial position modulation

Inhong Kim, Julien Leblanc, Philippe Moreau, Kwangseuk Kyhm, Aurélie Dupont, Irene Wang

Optical nanotopography of fluorescent surfaces by axial position modulation

INHONG KIM,[1,2] JULIEN LEBLANC,[1] PHILIPPE MOREAU,[1] KWANGSEUK KYHM,[2] AURÉLIE DUPONT,[1] AND IRENE WANG [1,*]

[1] *Univ. Grenoble Alpes, CNRS, LIPhy, 38000 Grenoble, France*
[2] *Department of Opto/Cogno-Mechatronics Engineering, Research Center for Dielectric Advanced Matter Physics (RCDAMP), Pusan National University, Busan 46241, Korea*
[*] *irene.wang@univ-grenoble-alpes.fr*

Abstract: We present an optical method that combines confocal microscopy with position modulation to perform axial tracking and topographic imaging of fluorescent surfaces. Using a remote focusing system, the confocal observation volume is oscillated in the axial direction. The resulting modulation of the detected signal is used as a feedback to precisely control the distance to an object of interest. The accuracy of this method is theoretically analyzed and the axial-locking accuracy is experimentally evaluated. Topographic imaging is demonstrated on fluorescently coated beads and fixed cells. This microscope allows for nanometric topography or tracking of dynamic fluorescent surfaces.

1. Introduction

Over the last decades, fluorescence microscopy has shed light on the spatio-temporal organization of living cells and tissues and has become a central tool for cell biology. With the traditional 200-nanometer spatial resolution of visible light and the associated temporal resolution on the order of milliseconds, it has been possible to follow the movement of vesicles or the dynamical rearrangements of the cytoskeleton, both of which occurring in quasi two dimensions. The third dimension is more difficult to address as the axial resolution is in general much inferior to the lateral one. A number of techniques, such as confocal microscopy or 3D localization microscopy, provide information in three dimensions but their temporal resolution is limited. Here, we focus on the difficulty to observe dynamical surfaces such as cellular membranes which are less than 10 nm in thickness and deforms as the cell morphology evolves, modifying the adherent structures for instance. Resolving and tracking the nanometer-scale topography of such biological surfaces is still a challenge.

The method of choice for measuring a topography at the nanometer scale, even in liquid, remains the Atomic Force Microscope [1–3]. This technique relies on the mechanical interactions between a solid tip and the probed surface. Hence, the surface of interest must be accessible and in the case of living cells, this restricts the use of AFM to measuring the nanotopography of the apical cytoplasmic surface. The Scanning Near-field Optical Microscopy (SNOM) methods work on the same principle but the interaction is mediated by light [4]. On the other side, the basal cytoplasmic membrane of adherent cells is optically accessible, for instance, with TIRF (Total Internal Reflection Fluorescence) microscopy. Due to the evanescent wave illumination, the axial position is encoded in the fluorescence intensity via an exponential dependency. The determination of the distance to the surface requires the knowledge of several parameters such as the local concentration of dyes, their orientation or the refractive index. Variations around the standard TIRF microscopy circumvent this difficulty. For instance, by acquiring a series of TIRF images obtained with different illumination angles, one can calibrate the system and obtain topography maps of the adherent membrane with a nanometric axial resolution [5]. Recently, Chizhik et al. [6] have taken advantage of the energy transfer from donor fluorophores and

metal surface plasmons to measure the topography of the basal membrane of living cells with a nanometer accuracy. More generally, a variety of approaches has been developed to push the axial precision to its limits, most of them belonging to the broad family of Single Molecule Localization Microscopy: e.g. Super-critical angle Fluorescence microscopy [7] or Points Accumulation for Imaging in Nanoscale Topography (PAINT) [8].

The main limitation of the above-mentioned techniques is that they are restricted to one surface (apical or basal) and cannot be applied to inner surfaces (e.g. the nuclear membrane). To break this barrier, one must rely on an all-optical strategy not based on any specific substrate-related phenomenon. To do so, we were inspired by the seminal work of J. Enderlein who proposed a feedback-based tracking method, namely the orbital tracking [9]. The principle is to continuously orbit a confocal spot around the fluorescent particle to track. When the particle is centered in the orbit, the fluorescent signal is constant. But, as soon as the particle has moved, a modulation appears at the frequency of the orbit. From the modulation amplitude and phase, the new position is calculated and the laser spot is centered again with a feedback loop. To obtain the third dimension, the idea is to measure in two planes slightly above and below the particle and to compare the corresponding intensities. For instance, Levi et al. alternated the axial position of the objective of a two-photon microscope to track beads [10]. Alternatively, Reuel et al. split the fluorescence signal onto two pinholes aligned on two different planes to track carbon nanotubes in 3D in living cells [11]. In order to study a larger object, live-cell microvilli, and measure the position of its fluorescent surface, Lanzano et al. decomposed the movement of the laser beam into: (i) a rapid oscillatory displacement to probe the local surface position and drive the feedback algorithm; and (ii) a lower frequency scanning around the whole closed surface [12–14]. The 3D shape of the moving microvillus is reconstructed from the known position of the laser and the distance from the surface with a nanometric accuracy.

Here, we want to measure the topography of any surface in living cells, closed like the nucleus membrane or open flat surfaces like parts of the cytoplasmic membrane. To do so, we go one step further and completely unravel the orbit. Hence, the laser spot is raster-scanned on the sample and simultaneously oscillated along the axial direction like the tip of an AFM in the tapping mode. As in the previous orbital methods, the real-time feedback of the intensity modulation allows to follow the shape of the fluorescent surface. This principle can be applied to tracking or topographic imaging applications. Since this method does not rely on the substrate's optical properties or on a solid object scanning the cell, in principle any fluorescent surface inside a transparent sample is accessible. In this work, the fast oscillating movement is achieved only along the axial direction, restricting the technique to nearly horizontal surfaces. But, there is no theoretical limitation to modulating at high frequency in any direction as in [12]. In this case, the approach presented here could be applied to any tilted or vertical surfaces. In the following, we present the theory of this nano-topographic imaging method and discuss the theoretical accuracy. Then, we show the practical implementation on model surfaces and finally on fixed cell membrane.

2. Principle of the method

In order to precisely determine the distance (along the axial direction z) to a fluorescent object of interest, we propose a method inspired by lock-in detection (Fig. 1). The confocal volume (product of the excitation and the detection efficiency distributions) is displaced along the axial direction in an oscillatory fashion at a given frequency. This causes the detected fluorescence signal to oscillate at the same frequency. By digital demodulation, the amplitude of the AC component, ΔF, can be extracted. The ratio of this amplitude to the average fluorescence level $\langle F \rangle$ is a function of the distance between the confocal volume and the object, independently of the level of fluorescence of the object. In the following, this modulation ratio will be named $m = \Delta F / \langle F \rangle$. Fig. 1 shows how the modulation ratio m depends on the distance along z, if the

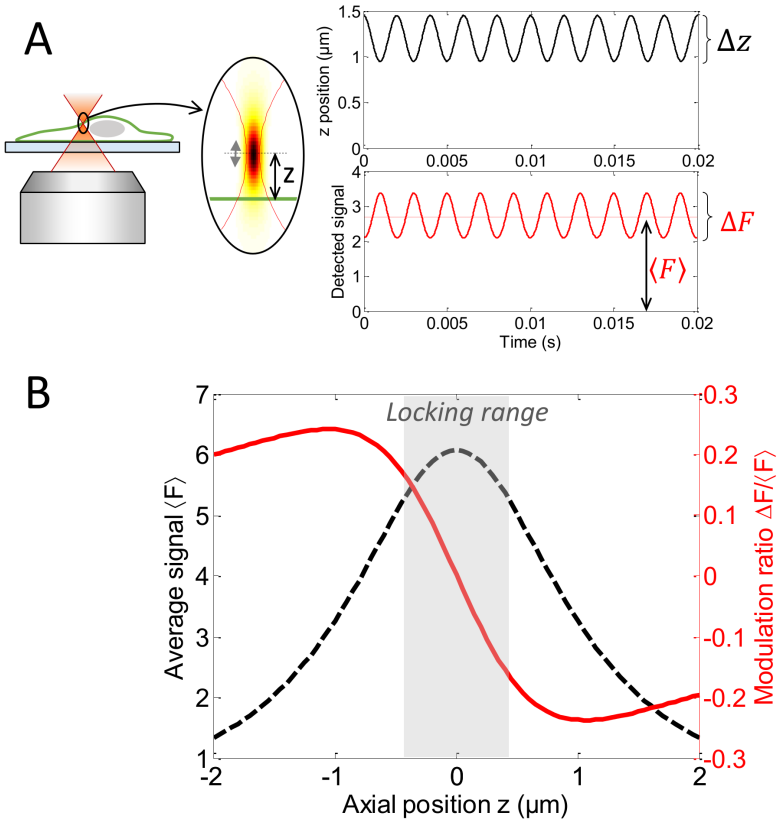

Fig. 1. Principle of nanotopography by axial modulation: (A) The microscope confocal volume is oscillated up and down in the vicinity of a fluorescent object (*e.g.* cell membrane), causing the detected fluorescence signal to be modulated with amplitude ΔF around its average $\langle F \rangle$. (B) Close to a fluorescent surface (at $z = 0$), the average signal (black dashed line) exhibits a peak while the modulation ratio (red line), defined as the amplitude of the first harmonic normalized by the average fluorescence, varies linearly with axial position, independently of the amount of fluorescence. Hence, using this information, axial localization and tracking can be performed.

object of interest is a fluorescent plane. The corresponding curves in the cases of a fluorescent point-like object and a fluorescent half-space are shown in the supplemental document.

As shown in Fig. 1, the modulation ratio m depends linearly on z position over a small range (approximately 1 μm in our case). Within this range, monitoring m yields a direct measurement of the z displacement, provided the slope is known, and enables to track a fluorescent structure in the axial direction in real time. The same procedure can be used to reconstruct the topography of a fluorescent structure: this is accomplished by confocal scanning in the x, y plane, while monitoring the height in z.

Hence this technique could be useful either for measuring the topography of relatively immobile structures or studying the dynamics of the mobile cell components (e.g. membrane of living cells) in the axial direction. It can also be combined with other techniques, such as fluorescence correlation spectroscopy [15], to follow a slowly moving structure of interest (*e.g.* the cell membrane) while measuring fast protein dynamics within this structure.

3. Theory and simulation

In this section, we present how the modulation ratio is expected to vary as a function of the axial position and theoretically predict the accuracy of the axial localization, in order to elucidate the role of various experimental parameters.

3.1. Modulation ratio as a function of axial position

First, in order to find out how the modulation ratio m depends on z, we express it using the confocal point spread function (PSF). Assuming small modulations, we write:

$$m = \frac{\Delta F}{\langle F \rangle} \approx \frac{\partial F}{\partial z} \frac{\Delta z}{\langle F \rangle} \tag{1}$$

where Δz is the amplitude of the position modulation around the average position z.

If we assume a perfectly axisymmetric PSF centered around the z-axis and that the fluorescence signal F is generated by a spatial distribution of fluorescence molecules given by $C(r, \phi, z)$ in cylindrical coordinates (where r is the radial distance, ϕ the azimuth and z the axial position), the fluorescence signal is

$$F(z) = F_0 \iiint C(r', \phi', z') \mathrm{PSF}(r', z - z') r' dr' d\phi' dz' \tag{2}$$

Now, we will consider the case of a fluorescent plane at $z = 0$ (the cases of a point-like emitter and a fluorescent half-space are presented in supplemental document). Moreover, a uniform distribution of fluorophores is assumed in the plane. Note that this assumption only needs to hold at the scale of the PSF for the below expression to be valid. Then F simplifies to (now F_0 has been changed to include the fluorophores density):

$$F(z) = F_0 \int_{r=0}^{\infty} \mathrm{PSF}(r', z) 2\pi r' dr' \tag{3}$$

In all the following, the shape of the PSF is assumed to be Gaussian-Lorentzian. Although this assumption is standard for two-photon microscopy [16], it would be rigorously valid for confocal microscopy *only* if the pinhole is infinitely small: in this case, the detection spatial efficiency is identical to the excitation efficiency, so that the confocal PSF is given by the square of the excitation intensity distribution. As the pinhole size is increased, the PSF elongates along its axis [17] but this variation cannot be described by a simple expression. Here, we choose to use a Gaussian-Lorentzian model, for the sake of simplicity:

$$\mathrm{PSF}(r, z) = \frac{1}{w_0^4 \left(1 + \left(\frac{z}{Z_R}\right)^2\right)^2} \exp\left[-\frac{4r^2}{w_0^2 \left(1 + \left(\frac{z}{Z_R}\right)^2\right)}\right] \tag{4}$$

w_0 is the waist and Z_R the Rayleigh length (i.e. the half-width at half maximum) of the illumination laser beam. Therefore, in the case of a fluorescent surface, the signal can be approximated by a Lorentzian function of z:

$$F(z) = \frac{\pi F_0}{4 w_0^2 \left(1 + \left(\frac{z}{Z_R}\right)^2\right)} \tag{5}$$

Hence the modulation ratio writes:

$$m(z) = -\frac{2z}{Z_R^2 + z^2} \Delta z \tag{6}$$

This expression confirms that the modulation ratio is independent of the fluorescence intensity but only depends on the oscillation amplitude and PSF shape. The slope of m in the vicinity of the fluorescent surface is $-2\Delta z/Z_R^2$. This slope is important as it determines the sensitivity of m to a change of z position and thus the accuracy of axial localization.

Note that the above derivation is only valid for small modulation amplitudes since it is based on local derivatives. In practice, as the modulation amplitude Δz is increased, the slope of m first increases, then it saturates and eventually drops for Δz larger than the PSF length. We simulated the modulation ratio m as a function of z for various modulation amplitudes, in the frame of the ideal Gaussian-Lorentzian PSF, by assuming a sinusoidal variation of $z(t)$ of frequency f, computing the fluorescence signal at each time point using Eq. 5 and extracting $\Delta F = 4\langle F(t)\cos(2\pi ft)\rangle$. The simulated variations of m (Fig. 2A) illustrates that the slope around $z = 0$ reaches a limit as Δz is increased. This limit is a function of the PSF axial length Z_R as shown in Fig. 2B: for smaller Z_R, a steeper slope can be reached. Further examination shows that the maximum slope value can be approximated by $-2/Z_R$ and is reached for a modulation amplitude of $\Delta z^{max} = 2 \times Z_R$ (see right side of Fig. 2B). Finally, the sensitivity of m to axial displacements is inversely proportional to the PSF axial length.

3.2. Localization accuracy

In order to predict the accuracy of z tracking, we estimate in the following the noise of the measurement of m in the case where experimental errors are limited by photon noise.

Let us consider that the confocal PSF is oscillated at frequency f. In consequence, the instantaneous count rate $F(t)$ is also modulated and can be expressed as (only the terms up to the first harmonic are considered): $F(t) = A_0 + A_f\cos(2\pi ft) + ...$ Since we defined the modulation ratio of the detected signal by $m = \Delta F/\langle F\rangle$, where ΔF is the peak-to-peak modulation amplitude at frequency f and $\langle F\rangle$ the count rate averaged over time, the modulation ratio is $m = 2A_f/A_0$. This is the quantity that we aim to measure.

In experiments, we record a series of photon counts I_k (with $k = 1, 2, ...$) each measured during a time interval $[t_{k-1}, t_k]$ of duration Δt. Hence the photon counts are related to the count rate by $I_k = F(t_k)\Delta t$. The total duration of one measurement T is assumed to be an integer number of modulation periods (which is the case in our experiments). To determine the modulation ratio, the continuous and modulated amplitudes are obtained by:

$$A_0 = \frac{1}{T}\sum_k I_k \tag{7}$$

$$A_f = \frac{2}{T}\sum_k I_k\cos(2\pi ft_k) \tag{8}$$

To express the variances of these two quantities, we will consider that the experimental uncertainty is limited by photon noise. Hence I_k follows a Poisson distribution, so that its variance is $\mathrm{var}(I_k) = I_k$. In addition, we assume that the noise on photon counts detected at different times are not correlated: this would allow us to write $\mathrm{var}(\sum_k I_k) = \sum_k \mathrm{var}(I_k)$.

$$\mathrm{var}(A_0) = \frac{1}{T^2}\mathrm{var}(\sum_k I_k) = \frac{1}{T^2}\sum_k \mathrm{var}(I_k) = \frac{1}{T^2}\sum_k I_k = \frac{A_0}{T} \tag{9}$$

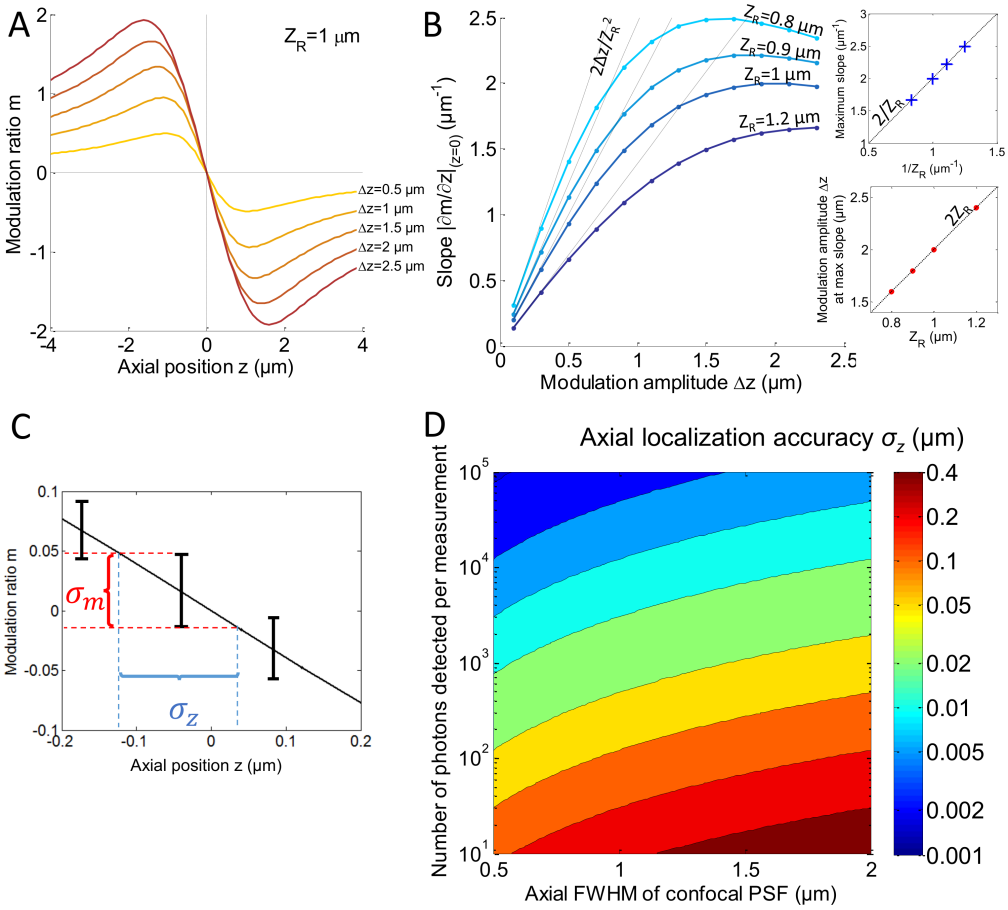

Fig. 2. Simulation of the modulation ratio and theoretical accuracy prediction: (A) Simulated modulation ratio around a fluorescent surface for various modulation amplitudes Δz (PSF length Z_R=1 μm): the slope becomes steeper as Δz increases up to a limit. (B) Slope (in absolute value) of the modulation ratio at $z = 0$ as a function of the modulation amplitude Δz for various PSF lengths Z_R. At small amplitudes, the slope increases linearly with Δz (light gray lines). Then it saturates to the value $2/Z_R$ (upper right graph) when Δz reaches $2Z_R$ (bottom right graph). (C) Illustration of how the accuracy of z localization (given by the standard deviation σ_z) depends on the measurement accuracy of m and the slope of m versus z. (D) Predicted axial localization accuracy (σ_z) as a function of the number of detected photons during one measurement and the axial FWHM of the confocal PSF.

$$\mathrm{var}(A_f) = \frac{4}{T^2}\sum_k \mathrm{var}(I_k)\cos^2(2\pi f t_k) \tag{10}$$

$$= \frac{4}{T^2}\sum_k I_k \cos^2(2\pi f t_k) \tag{11}$$

$$= \frac{4}{T^2}\left[A_0 \sum_k \cos^2(2\pi f t_k)\Delta t + A_f \sum_k \cos^3(2\pi f t_k)\Delta t\right] = \frac{2A_0}{T} \tag{12}$$

Now we need to express the variance of the modulation ratio,var(m), as a function of the variances

above (in first approximation, the uncertainties on A_0 and A_f are assumed to be independent).

$$\mathrm{var}(m) = \frac{4}{A_0^2}\mathrm{var}(A_f) + \frac{4A_f^2}{A_0^4}\mathrm{var}(A_0) + \frac{4}{A_0^4}\mathrm{var}(A_f)\mathrm{var}(A_0) \tag{13}$$

After replacing all quantities by their expression, we find:

$$\mathrm{var}(m) = \frac{8}{A_0 T} + \frac{4A_f^2}{A_0^3 T} + \frac{8}{A_0^2 T^2} \tag{14}$$

This variance can also be expressed using the total number of photons detected during a measurement that we note $N_{ph} = A_0 T$ and the modulation ratio itself:

$$\mathrm{var}(m) = \frac{8}{N_{ph}} + \frac{m^2}{N_{ph}} + \frac{8}{N_{ph}^2} \tag{15}$$

As expected, the uncertainty on the modulation ratio measurement decreases as the number of detected photons increases. Since the usual locking point is around $m = 0$ (PSF centered on the fluorescent surface), the dominant term in Equation 15 is the first one. Hence, a good approximation of the standard deviation of m is given by $\sigma_m \approx 2\sqrt{2}/\sqrt{N_{ph}}$.

To deduce the accuracy of z position estimation, as illustrated on Fig. 2C, the local slope of the dependence of m on z, obtained in the previous paragraph, has to be taken into account. In the case of a fluorescent surface, the maximum slope has been shown to scale as $dm/dz \approx -2/Z_R$, leading to the following estimation of the standard deviation of z:

$$\sigma_z = \frac{\sqrt{2} Z_R}{\sqrt{N_{ph}}} \tag{16}$$

Therefore, the axial localization accuracy depends on the PSF axial length and the number of detected photons. The theoretical accuracy is shown on Fig. 2D where σ_z is depicted as a function of the PSF axial dimension and the number of detected photons. For an easier interpretation, we chose to represent the PSF length by its FWHM (Full Width at Half Maximum) which is related to Z_R by $\mathrm{FWHM} = 2\sqrt{\sqrt{2}-1} Z_R \approx 1.3 Z_R$, in the case of our Gaussian-Lorentzian PSF model. According to Fig. 2D, with a FWHM of 1.15 μm (as estimated in our experiment), one needs to detect 4000 photons to reach an accuracy of 20 nm in axial localization. Only photon noise has been considered here, other instrumental noise could obviously increase the localization error.

4. Material and methods

4.1. Optical setup

Our setup is a custom-built confocal microscope, for both standard confocal imaging and z-modulation based topography or tracking. The optical layout is shown on Fig. 3. A 488-nm laser beam (85-BCD-020, CVI Melles-Griot - maximum power 20 mW) is reflected by a dichroic mirror (FF509-FDi02-t3, Semrock) and directed toward the Z modulation module. Axial oscillation of the confocal volume is performed by a remote focusing setup: after reflection by a polarizing beamsplitter (PBS), a high numerical aperture objective (UPlanApo ×60, NA=0.90, Olympus) focuses the beam onto a mirror (7 mm-diameter protected silver, Thorlabs) placed on a piezoelectric actuator (Z stage with 5 μm travel range, Piezoconcept). The reflected beam's polarization is rotated by 90°, thanks to the insertion of a quarter-wave plate, so that the output is transmitted by the PBS. A pair of relay lenses (L_1, L_2) conjugates this objective' pupil plane to the middle plane between two galvanometric scanners (6215H, Cambridge Technology). The

beam is then directed toward an inverted microscope stand (Olympus IX-70). A second relay, consisting of the scan lens (L_3) and the microscope tube lens, conjugates the galvo scanners with the imaging objective (UPlanSApo, ×60, NA=1.2, water-immersion, Olympus) pupil plane. This latter objective is mounted on a piezoelectric Z positioner (FOC, Piezoconcept) of 100 μm travel range, which is used for acquiring confocal z-stacks and follow the surface during topographic imaging.

As recommended in Ref. [18], the relay lenses were chosen to match, as well as possible, the pupils of the two objectives (Z modulation and imaging) in both position and size, in order to compensate for spherical aberrations that appear when objective work out of their focal plane. However, the small displacements required for Z modulation in our case (less than 2 μm) significantly mitigate this problem. Also note that, although the Z modulation objective has a lower NA (0.9) than the imaging objective (1.33), since it operates in air, its *angular aperture* is similar, so that it does not restrict the resolution of the overall microscope.

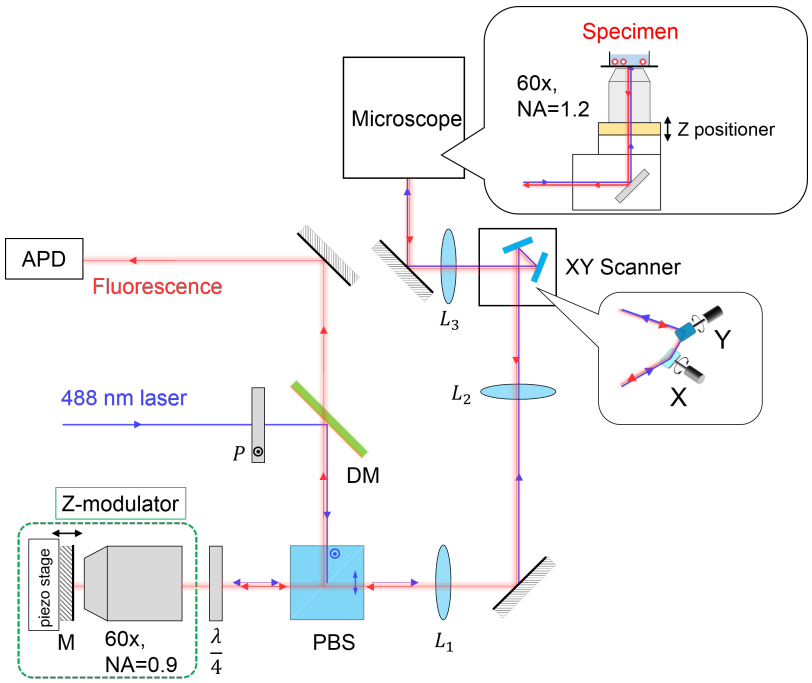

Fig. 3. Experimental setup: a Z-modulation module (green dashed box), consisting of an objective and a mirror on a piezoelectric stage, is added on both the excitation and emission paths of a scanning confocal microscope. Oscillation of the mirror M (of typical amplitude 1 μm) causes the PSF in sample space to oscillate up and down. The modulated fluorescence signal is detected by an avalanche photodiode. A piezoelectric Z positioner mounted under the imaging objective is used to follow the object's axial displacement. A galvanometric XY scanner allows imaging by point scanning. (P: polarizer, DM: dichroic mirror, PBS: polarizing beamsplitter, M: mirror, APD: avalanche photodiode, L_1: achromatic doublet (f_1=180 mm), L_2: achromatic doublet (f_2=75 mm), L_3: set of two 125 mm-focal length doublets resulting in a equivalent focal length of f_3=62.5 mm.)

The axial displacement of the confocal PSF (in the sample space) is given by $Z = 2Z_M/n_w$ for a displacement of the piezo-actuated mirror of Z_M (with n_w the refractive index of water), since the Z modulation objective and the imaging objective have the same focal distance but different

immersion media. The factor 2 is due to the fact that the image reflected by a mirror is displaced by twice the mirror's axial displacement. Therefore, $Z \approx 1.5 Z_M$. The actual displacement amplitude of the mirror (for a given control voltage) has been calibrated using the sensor signal of the piezo stage as a function of the frequency: the maximum amplitude varies from 5 μm for frequencies below 100 Hz to 0.3 μm at 2 kHz. The measurements presented here were performed at 200 Hz where a factor 0.85 is found between the command and the actual displacement.

The fluorescence emission follows the exact same path back through the galvanometric mirrors and the Z modulation module (*descanned* configuration). It is transmitted by the dichroic mirror and detected through a 25 μm-core step-index multimode fiber (acting as the confocal pinhole) by an avalanche photodiode (APD) module (SPCM-AQRH-13, Perkin Elmer). This descanned configuration results in half of the emitted fluorescence light being lost in the Z modulation module. In spite of that, this configuration allows better stability of the confocal PSF since excitation and detection volumes stay overlapped at all times, which prevents any distortion of the PSF during axial oscillation.

All instruments (piezoelectric stage and Z positioner, galvanometric motors) are controlled using a multi-function acquisition board (PCIe-6343, National Instruments) which also detects the counts from the APD module. A custom Python script was developed to perform the acquisitions. Each measurement entails acquiring the fluorescence over a few periods of oscillation and computing the modulation ratio on the CPU. Starting the acquisition and transferring the data generates an overhead of 4 ms for each measurement point. Therefore, our system is presently limited to relatively slow imaging or tracking speeds. Faster control could be achieved by using a FPGA that enables on-board computing, for example.

4.2. Test samples

For accuracy assessment, we used a layer of dried dye solution: we poured 200 μl of an aqueous solution of Rhodamine 6G (~0.1 μM) dry in a glass-bottom well (LAB-TEK 8-well slide) and let it dry.

As a model sample for topography measurement, we used biotin-coated microspheres of size between 8 and 13 μm (TPX-100-5, Spherotech) labeled with AlexaFluor488-streptavidin conjugated fluorophores [4]. First, a solution containing 500 μl of water, 500 μl of PBS, 30 μl of stock microspheres solution and 1 μl of streptavidin-functionalized AF488 (Life Technologies, S32354) was prepared. The solution was centrifuged during 30 minutes at 10 krpm and the liquid phase was removed and replaced with 100 μl of PBS. Then, the solution was vortexed in order to dissolve the deposit. Finally, 1 ml of PBS was added to 50 μl of the solution on the coverslip. We waited at least 1 hour before starting the acquisitions.

4.3. Fixed cells

The method was tested on fixed cells with fluorescently labelled membrane. NIH3T3 cells were stained with CellMask™(Life Technologies) then fixed with PFA. All protocols were carried according to the manufacturer's recommendations.

5. Experimental results

5.1. Tracking noise

The aim of this section is to validate experimentally the theoretical predictions presented in section 3. As a sample, we used a dried layer of fluorescent dye (Rhodamine 6G).

First, in order to compare experimentally measured modulation ratios with simulations, we measured the axial length of the confocal PSF on our setup by scanning the imaging objective in the axial direction, across the fluorescent layer. The detected signal as a function of z position, shown on Fig. 4A, can be correctly approximated by our Gaussian-Lorentzian model (Eq. 5) with

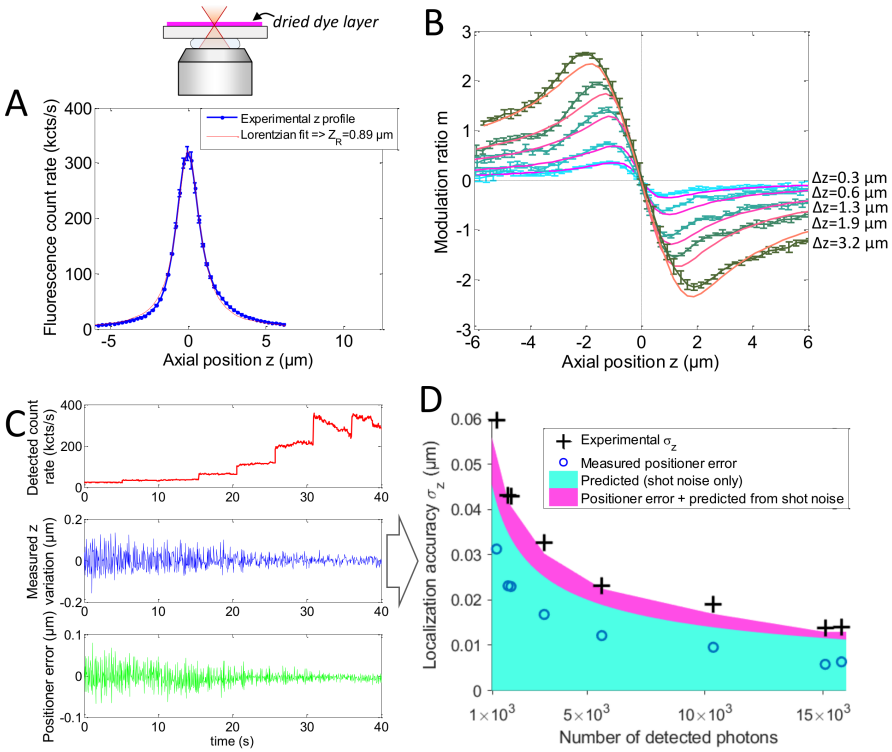

Fig. 4. Experimental accuracy assessment: (A) Fluorescence count rate detected when scanning through a dried Rhodamine 6G layer (at z=0). Average of 5 scans at different locations on the layer with standard deviations depicted as error bars (blue dotted line). The fit (red line) provides an estimation of the PSF elongation Z_R. (B) Measured modulation ratio as a function of the distance to the dye layer for various PSF oscillation amplitudes (Δz= 0.3, 0.6, 1.3, 1.9 and 3.2 μm). At each oscillation amplitude, 5 acquisitions at different locations on the sample were averaged (s.d. shown as error bars). Simulated modulation ratios (magenta to orange lines), calculated with a Gaussian-Lorentzian PSF (of Z_R=0.89 μm) and without free parameters, are consistent with experimental values. (Measurements carried with 200 Hz oscillation frequency, 40 periods for each point.) (C) Z tracking experiment with increasing laser power: detected count rate (red line in upper panel), fluctuations of the measured z position (blue line in middle panel) and difference between target and actual positions of the objective Z positioner (green line in lower panel) as a function of time. (oscillation frequency 200 Hz and amplitude Δz=1.8 μm - 10 periods are acquired for each m measurement, *i.e.* 50 ms per point.) (D) Localization error σ_z (standard deviation of 100 position measurements) as a function of the number of detected photons. The experimental values (black crosses) cannot be explained by the predicted accuracy if only shot noise is taken into account (cyan patch), but is well matched if the measured positioning error (blue circles) is added to shot-noise-induced error (magenta patch).

Z_R=0.89 μm. This value is large compared to what is expected of an ideal confocal microscope with this pinhole size (around 0.4 airy units) [17, 19], which should lead to $Z_R \approx$0.5 μm. We believe this discrepancy is mainly due to spherical aberrations induced by the Z modulation objective (its coverslip-thickness correction does not correspond to our configuration), which results in an elongated PSF.

Using the measured PSF length, we found that experimental modulation ratios closely match the simulated curves, for various amplitudes of modulation Δz ranging from 0.3 μm to 3.2 μm (Fig. 4B). In spite of a slight asymmetry in the experimental curves, the slope at $z = 0$ is in good agreement with the simulations.

Then we performed axial tracking: at each loop, the modulation ratio m is measured; its deviation from the target value (usually m_{target}=0) is calculated and converted into an axial displacement, using the known slope; this provides a measurement of the object's z position which is then sent to the objective Z positioner, so that it can follow the displacement of the object. At each loop, we record the fluorescence count rate, the measured object position, and the Z positioner's sensor signal that indicates its actual position.

As the dye layer is immobile, the variations of z position provide an estimation of the accuracy of localization. To measure this accuracy as a function of the number of detected photons, we varied the laser power in steps, as shown on Fig. 4C. The detected count rate also increases in steps, although photobleaching can be observed for higher power values (Fig. 4C,upper graph). As more photons are detected, the variability of measured z positions is visibly reduced (Fig. 4C, middle graph). The difference between the target position sent to the Z positioner and its real position is depicted in the bottom part of Fig. 4C and reveals the positioning error.

Fig. 4D shows the localization accuracy σ_z, given by the standard deviation calculated over 100 measured z values, as a function of the number of detected photons, calculated from the average count rate on the same interval. The error on the measured z position may result from two main causes: the uncertainty due to shot noise, given by $\sigma_z^{shot} \approx 2\sqrt{2}/(\sqrt{N_{ph}}|\partial m/\partial z|)$ (as detailed in section 3), and the error of the Z positioner (measured from its sensor signal). By adding the variances of these two independent contributions, we found uncertainty values consistent with the experimental σ_z (Fig. 4D).

5.2. Topographic imaging

To demonstrate topographic imaging with our technique, AlexaFluor488-coated polystyrene spheres of 10 μm diameter were imaged. An example of such a sphere is shown on Fig. 5. We first recorded a confocal stack around the sphere to determine its radius (since the size of these spheres can vary between 8 and 11 μm): the image on the equatorial plane is shown on Fig. 5A, providing an estimated radius of 10.4 μm for this particular sphere.

Then we moved to the bottom surface. The slope of m as a function of z was calibrated by an initial axial scan through the fluorescent surface. A topographic image was then acquired: galvanometric mirrors are used to scan the confocal PSF in the (x,y) plane; at each pixel, the fluorescence signal is measured over a few oscillation periods and its modulation ratio yields the z position of the sphere's surface, which becomes the target position for the objective Z positioner. At each pixel, both the z position, which provides the topographic image depicted on Fig. 5B, and the fluorescence signal (Fig. 5C) are recorded. The latter is relatively homogeneous, indicating that the sphere surface is uniformly coated with the fluorophores, with a slight decrease in the center presumably due to photobleaching during the initial axial scan.

The topographic image can be fitted with the model of a sphere (Fig. 5D), yielding an estimated radius (R=5.16 μm) in good agreement with the one deduced from the image in the equatorial plane. The fit residual (Fig. 5D) provides an estimation of the axial accuracy, which is ~40 nm. Since the number of photons detected per measurement is around 2500 (50 ms acquisition of an average signal of 50 kCts/s), this noise level is in reasonable agreement with the tracking noise measured above (Fig. 4D). The slightly higher noise observed here may be due to increased mechanical instabilities compared to the case of the immobile sample.

An example of topographic imaging on a fixed cell is shown on Fig. 6. The cell membrane was fluorescently labelled. We performed topographic imaging in an area that includes part of the cell nucleus. An axial scan recorded over the nucleus (Fig. 6C) clearly shows two separate

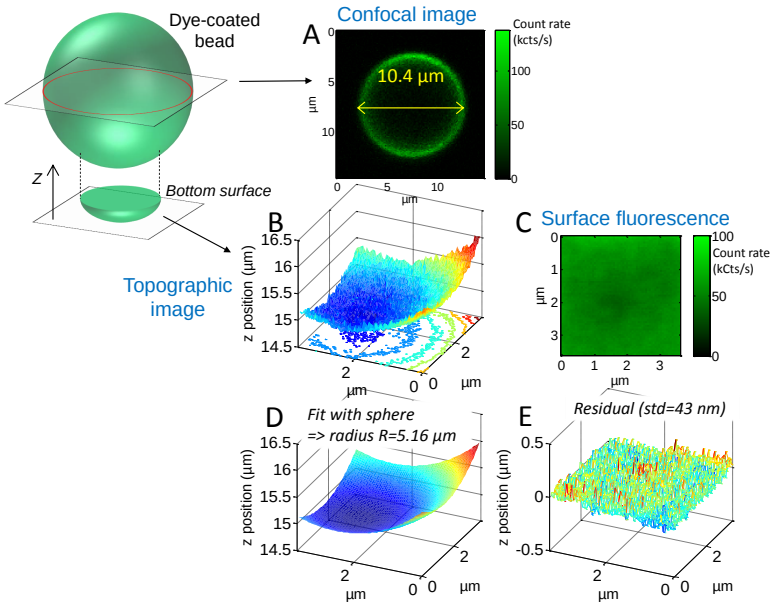

Fig. 5. Topographic imaging on surface-coated spheres: (A) Confocal image of a AlexaFluor488-coated polystyrene sphere extracted from a Z stack: the equatorial plane provides a measure of the sphere diameter, here 10.4 μm (128×128 pixels - 0.1 μm/pixel.) (B) Topographic image of the same sphere (64×64 pixels, pixel size 0.08 μm, oscillation amplitude Δz=1.3 μm, frequency 200 Hz, 10 periods per point.) (C) Corresponding average fluorescence signal recorded during topographic imaging. (D) Sphere model that fits the topographic data using center coordinates and radius as free parameters. The estimated radius, 5.16 μm, is very close to the expected value from the confocal image. (E) Fit residuals. The standard deviation of the residual gives an estimation of z measurement accuracy. (Measurements carried with 0.4 μW laser power at imaging objective.)

peaks on the average signal, when the PSF crosses the ventral membrane (close to the substrate) then the dorsal one (second peak). In the vicinity of each membrane, the modulation ratio sharply drops. We chose to lock at the middle of the second drop, corresponding to the dorsal membrane. Then we performed topographic imaging: the average fluorescent signal and z position measured simultaneously are shown on Fig. 6B and D. The topography shows a clear ~2 μm-high protuberance above the nucleus. The fluorescence image exhibits lower intensity over the nucleus, and clustered structures beside the nucleus. These latter may be due to internalization of the dye used to label the membrane. Care must be taken when considering the measured surface fluorescence, since it may be biased by the locking efficiency at each position (which depends on the slope of the modulation ratio at this point). However our data shows that this approach can provide topographic information on the dorsal membrane, above compartments of the cell with different fluorescence properties.

6. Conclusion

We presented an all-optical microscope for topographic imaging and tracking. It consists in inducing a modulation of the fluorescence signal by moving the confocal volume in an oscillatory manner along the optical axis. The signal modulation ratio provides a measure of the distance of the fluorescent object to the imaging plane. We showed that the accuracy of the

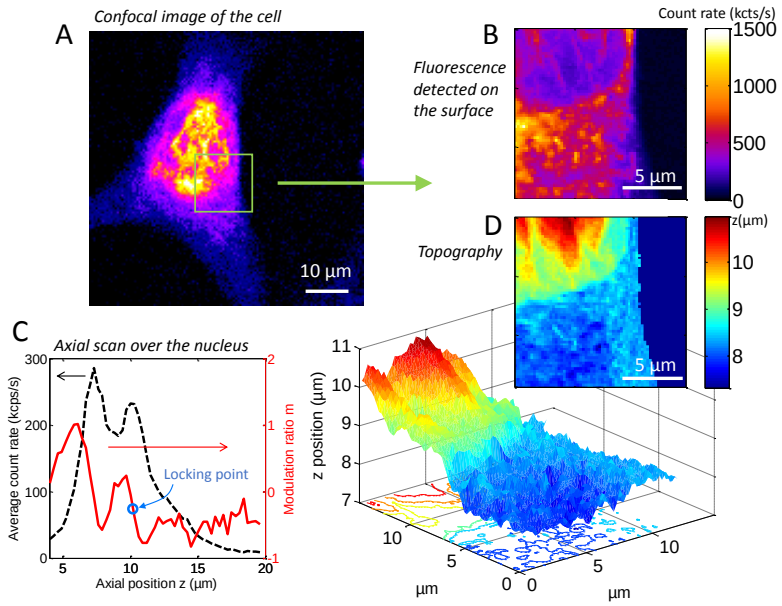

Fig. 6. Topographic imaging on fixed cell: (A) Standard confocal image of the cell, the green square corresponds to the area imaged in topography. (B) Average fluorescence signal recorded during topographic imaging. (C) Average signal (black dashed line) and modulation ratio (red line) measured as a function of axial position, at the upper-left corner of the area imaged in topography. The two peaks in the signal correspond to the ventral and dorsal membrane, respectively. The locking-point (blue circle) was placed on the dorsal membrane. (D) Measured topography of the dorsal membrane depicted as a 3D surface (bottom) and an image (top right), showing a protuberance over the nucleus (64×64 pixels, pixel size 0.2 μm, oscillation amplitude Δz=1.3 μm, frequency 200 Hz, 5 periods per point, laser power 5 μW at objective entrance.)

axial localization depends on the number of detected photons and the axial resolution of the microscope. Predicted accuracy values were found to be consistent with experiments. Finally, we demonstrated topographic imaging on model samples, surface-coated polystyrene sphere, and membrane-stained cells. In terms of resolution, our technique is not limited by optical diffraction, since an axial 'resolution' of a few tens of nanometers can be readily achieved.

The setup described here could be improved in future work. First, the axial resolution of this microscope is impaired by spherical aberrations: we expect a more careful choice of the remote focusing objective would allow to reduce the axial elongation of the confocal PSF and, hence, the z localization accuracy by up to a factor of 2. Another issue is the measurement speed: 20 to 50 ms is presently needed for each z measurement. This is due to two limitations: the overhead when transferring the data from the acquisition board to the computer, which could be solved by on-board computing using an FPGA, and the mechanical response of the objective Z positioner. This latter device moves the objective to follow the fluorescent object of interest, but is relatively slow due to its heavy load. A solution would be to use remote focusing, not only for small amplitude oscillations, but also for long-range focus displacements. Note that, although our system is presently too slow for live topographic imaging, it may be compatible with tracking applications that are not so demanding in terms of speed.

This method can be applied to study cell apical membranes and internal surfaces with high axial accuracy, as opposed to optical methods (TIRF,...) that operate close to the substrate. In particular, combining this method with fluorescence correlation spectroscopy (FCS), for example,

would enable to stay locked on a surface of interest (e.g. cell membrane), while measuring molecular mobility within this surface.

Funding. This research was supported by a grant of the Korea Health Technology R&D Project through the Korea Health Industry Development Institute (KHIDI), funded by the Ministry of Health & Welfare, Republic of Korea (grant number: HI19C1085). The project has started thanks to a funding of the MITI (CNRS, "Instrumentation aux limites", project Nanotopo).

Disclosures. The authors declare no conflicts of interest.

Data availability. Data underlying the results presented in this paper are not publicly available at this time but may be obtained from the authors upon reasonable request.

Supplemental document. See Supplement 1 for supporting content.

References

1. H. J. Butt, E. K. Wolff, S. A. C. Gould, B. Dixon Northern, C. M. Peterson, and P. K. Hansma, "Imaging cells with the atomic force microscope," J. Struct. Biol. **105**, 54–61 (1990).
2. C. Rotsch and M. Radmacher, "Drug-Induced Changes of Cytoskeletal Structure and Mechanics in Fibroblasts: An Atomic Force Microscopy Study," Biophys. J. **78**, 520–535 (2000).
3. F. Eghiaian, A. Rigato, and S. Scheuring, "Structural, Mechanical, and Dynamical Variability of the Actin Cortex in Living Cells," Biophys. J. **108**, 1330–1340 (2015).
4. T. Enderle, T. Ha, D. Ogletree, D. Chemla, C. Magowan, and S. Weiss, "Membrane specific mapping and colocalization of malarial and host skeletal proteins in the plasmodium falciparum infected erythrocyte by dual-color near-field scanning optical microscopy," Proc Natl Acad Sci USA **94**, 520– (1997).
5. M. Cardoso Dos Santos, R. Déturche, C. Vézy, and R. Jaffiol, "Topography of Cells Revealed by Variable-Angle Total Internal Reflection Fluorescence Microscopy," Biophys. J. **111**, 1316–1327 (2016).
6. A. I. Chizhik, J. Rother, I. Gregor, A. Janshoff, and J. Enderlein, "Metal-induced energy transfer for live cell nanoscopy," Nat. Photonics **8**, 124–127 (2014).
7. C. M. Winterflood, T. Ruckstuhl, D. Verdes, and S. Seeger, "Nanometer Axial Resolution by Three-Dimensional Supercritical Angle Fluorescence Microscopy," Phys. Rev. Lett. **105**, 108103 (2010).
8. A. Sharonov and R. M. Hochstrasser, "Wide-field subdiffraction imaging by accumulated binding of diffusing probes," Proc. Natl. Acad. Sci. **103**, 18911–18916 (2006).
9. J. Enderlein, "Tracking of fluorescent molecules diffusing within membranes," Appl. Phys. B **71**, 773–777 (2000).
10. V. Levi, Q. Ruan, and E. Gratton, "3-D particle tracking in a two-photon microscope: application to the study of molecular dynamics in cells." Biophys. J. **88**, 2919–2928 (2005).
11. N. F. Reuel, A. Dupont, O. Thouvenin, D. C. Lamb, M. S. Strano, B. N. F. Reuel, A. Dupont, O. Thouvenin, D. C. Lamb, and M. S. Strano, "Three-dimensional tracking of carbon nanotubes within living cells." ACS Nano **6**, 5420–5428 (2012).
12. L. Lanzano, M. A. Digman, P. Fwu, H. Giral, M. Levi, and E. Gratton, "Nanometer-scale imaging by the modulation tracking method," J. Biophoton. **4**, 415–424 (2011).
13. L. Lanzano and E. Gratton, "Measurement of distance with the nanoscale precise imaging by rapid beam oscillation method," Microsc. Res. Tech. **75**, 1253–1264 (2012).
14. C.-L. Chiu, C. Tsai, G. Wu, E. Gratton, J. Aguilar, and M. Digman, "Nanoimaging of Focal Adhesion Dynamics in 3D." PLoS One **9**, e99896 (2014).
15. E. Haustein and P. Schwille, "Fluorescence correlation spectroscopy: Novel variations of an established technique," Annu. Rev. Biophys. Biomol. Struct. **36**, 151–169 (2007).
16. K. Berland, P. So, and E. Gratton, "Two-photon fluorescence correlation spectroscopy: method and application to the intracellular environment," Biophys. J. **68**, 694–701 (1995).
17. T. Wilson, "Optical sectioning in confocal fluorescent microscopes," J. Microsc. **154**, 143–156 (1989).
18. E. Botcherby, R. Juškaitis, M. Booth, and T. Wilson, "An optical technique for remote focusing in microscopy," Opt. Commun. **281**, 880–887 (2008).
19. T. Wilson, "Resolution and optical sectioning in the confocal microscope," J. Microsc. **244**, 113–121 (2011).